2014

Blind modal identification of structures from spatially sparse seismic

S. F. Ghahari
Sharif University of Technology

F. Abazarsa
International Institute of Earthquake Engineering and Seismology

M. A. Ghannad
Sharif University of Technology

M. Celebi
ESC, USGS

E. Taciroglu
Civil and Environmental Engineering Department

Blind modal identification of structures from spatially sparse seismic response signals

S. F. Ghahari[1], F. Abazarsa[2], M. A. Ghannad[1], M. Çelebi[3] and E. Taciroglu[4,*,†]

[1]*Department of Civil Engineering, Sharif University of Technology, Tehran, Iran*
[2]*Structural Engineering Department, International Institute of Earthquake Engineering and Seismology, Tehran, Iran*
[3]*ESC, USGS, Menlo Park, CA 94025, U.S.A.*
[4]*Civil and Environmental Engineering Department, UCLA, Los Angeles, CA 90095, U.S.A.*

SUMMARY

Response-only identification of civil structures has attracted much attention during recent years, as input excitations are rarely measurable for ambient vibrations. Although various techniques have been developed by which identification can be carried out using ambient responses, these techniques are generally not applicable to non-stationary excitations that structures experience during moderate-to-severe earthquakes. Recently, the authors proposed a new response-only modal identification method that is applicable to strong shaking data. This new method is highly attractive for cases in which the true input motions are unavailable. For example, when soil–structure interaction effects are non-negligible, neither the free-field motions nor the recorded foundation responses may be assumed as input. Even in the absence of soil–structure interaction, in many instances, the foundation responses are not recorded (or are recorded with low signal-to-noise ratios). Thus far, the said method has been only applicable to fully instrumented systems wherein the number of sensors is equal to or greater than the number of active modes. In this study, we offer various improvements, including an extension that enables the treatment of sparsely instrumented systems. Specifically, a cluster-based underdetermined time–frequency method is employed at judiciously selected auto-source points to determine the mode shapes. The mode shape matrix identified in this manner is not square, which precludes the use of simple matrix inversion to extract the modal coordinates. As such, natural frequencies and damping ratios are identified from the recovered modal coordinates' time–frequency distributions using a subspace method. Simulated data are used for verifying the proposed identification method. Copyright © 2013 John Wiley & Sons, Ltd.

Received 4 February 2013; Revised 18 June 2013; Accepted 1 July 2013

KEY WORDS: blind identification; output-only identification; sparse instrumentation; seismic response; time–frequency distributions

1. INTRODUCTION

Identification of the modal characteristics of civil structures—that is, natural frequencies, damping ratios, and mode shapes—from response signals recorded during strong ground shaking has been a subject of research for more than three decades [1–3]. However, when there is soil–structure interaction, signals recorded at the foundation level during ground shaking are different from the true foundation input motions [4,5]. In such cases, neither the methods that require knowledge of the input [6,7] nor the methods that assume the input to be white noise [8–10] can be used.

Recently, a new output-only identification method has been developed for civil structures by Ghahari *et al.* [11]. This method obviates the need for the unknown input to be uncorrelated and works in two steps. First, the mode shapes and modal coordinates are extracted by applying a blind source separation (BSS) technique [12,13] to the spatial time–frequency distribution (STFD) matrices of the

*Correspondence to: E. Taciroglu, Civil and Environmental Engineering Department, UCLA, Los Angeles, CA 90095, U.S.A.
†E-mail: etacir@ucla.edu

recorded responses. BSS has recently attracted much attention from researchers in the civil engineering community who seek to use it in modal identification and structural health monitoring applications [14–24]. Then, natural frequencies and damping ratios are identified through concurrent analyses of the extracted modal coordinates. Although it was demonstrated that this method could be successfully employed for output-only identification of civil structures under non-stationary earthquake excitations, its application was limited to determinate and overdetermined cases in which the number of active modes is equal to or smaller than the number of sensors.

In the present study, we propose an extension through which only a few response signals are used for identification. Multiple-input excitations and closely spaced modes—two limitations of the previously proposed method—are also addressed here. In the first step of this new approach, time–frequency (TF) points at which only one mode is present are identified through a new auto-source point selection criterion. Second, a cluster-based underdetermined TF BSS method [25] is employed to extract real-valued mode shapes, because the modes are assumed to be completely disjoint at the selected auto-source points. Note that one of the remaining limitations is that the mode shapes are assumed to be real valued, whereas there exists real-life cases—for example, long and flexible or lightly damped structures—that exhibit complex modes. Nevertheless, the method proposed here can be extended by adopting an approach similar to what was proposed in [26,27]. The mode shape matrix identified in this manner is not square, which precludes the use of simple matrix inversion to extract the modal coordinates. As such, the natural frequencies and damping ratios must be identified from the recovered modal coordinates' time–frequency distributions (TFDs). Hence, a subspace-based method [28] is used to recover the modal coordinates' TFDs. Through this approach, it is now possible to extract modal coordinates' TFDs even for TF points at which several modes are present simulta-neously, that is, non-disjoint modes. This capability is quite attractive for applications on civil structures that have closely spaced modes. After recovering the modal coordinates' TFDs, natural frequencies can be identified as frequency lines with maximum energy. Damping ratios of several modes can also be identified from the free vibration portions of the recovered modal coordinates' TF representations. The method does not depend upon the number of input motion excitations—that is, it is applicable, for example, to soil–structure systems under both sway and rocking input motions.

The remainder of this manuscript is organized as follows. The proposed identification method is presented in Section 2, in which the mode shape, natural frequency, and damping ratio identification approaches are presented in three successive subsections. In Section 3, the performance of the proposed method is addressed using a synthetic data set from a 10-story building. Finally, concluding remarks are provided in Section 4.

2. PROPOSED IDENTIFICATION TECHNIQUE

2.1. A blind source separation approach to system identification

The governing equations of motion for an N-DOF system with n instrumented DOFs, which is excited by q input accelerations, can be expressed as

$$\mathbf{M}\ddot{\boldsymbol{x}}(t) + \mathbf{C}\dot{\boldsymbol{x}}(t) + \mathbf{K}\boldsymbol{x}(t) = -\mathbf{M}\mathbf{l}\ddot{\boldsymbol{x}}_g(t) \tag{1}$$

where $\mathbf{M}$, $\mathbf{C}$, and $\mathbf{K}$ are the constant $N \times N$ mass, proportional damping, and stiffness matrices of the system, respectively. The vector $\boldsymbol{x}(t)$ contains relative displacement responses of the system at all DOFs; $\ddot{\boldsymbol{x}}_g(t) = \left[\ddot{x}_{g1}(t) \cdots \ddot{x}_{gq}(t)\right]^T$ is a vector time signal, which contains the (unknown) foundation input accelerations; and $\mathbf{l}$ is the influence matrix [29]. The absolute acceleration of structure is

$$\ddot{\boldsymbol{x}}^t(t) = \ddot{\boldsymbol{x}}(t) + \mathbf{l}\ddot{x}g(t), \tag{2}$$

which can be expressed in modal space as

$$\ddot{\boldsymbol{x}}^t(t) = \boldsymbol{\phi}\ddot{\boldsymbol{q}}(t) \tag{3}$$

where $\boldsymbol{\phi}$ is an $N \times m$ real-valued mode shape matrix whose i-th column ($\boldsymbol{\phi}_i$) is the i-th mode shape and $\ddot{\boldsymbol{q}}(t)$ is a vector that contains the *absolute acceleration* modal coordinates whose i-th row is the

absolute acceleration response of an SDOF system with the natural frequency, ω_n, and damping ratios, ξ, corresponding to the i-th mode. Also, $m \leq N$ is the number of contributing modes.

It is expedient to note here that Equation (3) is similar to the basic equation in BSS [30] techniques, in which an attempt is made to recover both the mixing matrix (here, the mode shape matrix) and the source signals (here, the modal coordinates) from the response signals. Herein, based on the TF domain BSS technique developed by Belouchrani et al. [12,13], we propose a technique to estimate the modal coordinates ($\ddot{q}(t)$) and the mode shape matrix (ϕ), using a limited number of recorded response signals ($\ddot{x}^t(t)$). This type of BSS problem is usually referred to as *underdetermined* problems [31]; that is, the number of sensors is less than the number of sources. The recovery of the modal coordinates is an additional challenge, because mode shape matrix is not square. The key ingredient for solving these underdetermined problems is the exploitation of the sparseness of the source signals [32]. To that end, response signals are usually transformed to domains in which the source signals are disjoint or quasi-disjoint. The TF domain is the most suitable domain for non-stationary source signals, wherein several studies have attempted to tackle underdetermined problems [25–28,33,34].

Here, we present a new method wherein the mode shapes are identified first through a cluster-based method described in [25] from TF points at which the modal coordinates are completely disjoint. Then, modal coordinates' TFDs are recovered from all TF points by a method proposed in [28], which is a subspace-based method for non-disjoint sources.

Calculating the STFD of both sides of Equation (3) yields

$$\mathbf{D}_{\ddot{x}^t \ddot{x}^t}(t,f) = \phi \mathbf{D}_{\ddot{q}\ddot{q}}(t,f) \phi^T \tag{4}$$

where $\mathbf{D}_{\ddot{x}^t \ddot{x}^t}(t,f)$ and $\mathbf{D}_{\ddot{q}\ddot{q}}(t,f)$ are, respectively, $n \times n$ and $m \times m$ ($n < m$) STFD matrices whose elements are the auto-TFD and cross-TFD of the recorded signals and the modal coordinates, and T denotes matrix or vector transpose. The discrete-time form Cohen-class STFD matrix of a vector x containing n analytic signals is defined as [35]

$$\mathbf{D}_{xx}(t,f) = \sum_{l=-\infty}^{+\infty} \sum_{m=-\infty}^{+\infty} \varphi(m,l)\, x(t+m+l)\, x^H(t+m-l)\, e^{-4\pi jfl} \tag{5}$$

where $[\mathbf{D}_{xx}(t,f)]_{kl} = D_{x_k x_l}(t,f)$ for $k,l \in \{1,\dots,n\}$. Here, the superscript H denotes a Hermitian transpose, and $j = \sqrt{-1}$. The scalars t and f represent the time and frequency variables, respectively. Different choices of the kernel function, $\varphi(m,l)$, which depends on both the time (t) and the lag (l) variables, lead to different TFD realizations. These quadratic TFDs have higher TF resolutions than linear ones—for example, short time Fourier transform—but suffer from interference. Interference terms are spurious features that appear when representing a multi-component signal in the TF domain using one of the quadratic methods, while points corresponding to the true energy are named auto-terms. A new TFD family, which is referred to as reduced interference distribution (RID), has been proposed [36] to attenuate the interference terms. Herein, we adopt the *smoothed pseudo Wigner–Ville distribution* (SPWVD) [37], which is an enhanced version of *Wigner-Ville distribution* (WVD) [38] and belongs to the said RID family.

Considering the STFD definition provided earlier, and by assuming that an ideal TF distribution tool (such as SPWVD) is utilized so that the interference terms have been reduced, the TF points can now be classified into three different groups based on the localization of modal coordinates observed in earthquake engineering as follows:

1. *Single auto-term TF point* (SATFP): At these points, only one mode is present; thus, STFD matrices of modal coordinates, $\mathbf{D}_{\ddot{q}\ddot{q}}(t,f)$, are diagonal with only one non-zero diagonal element, which represents the energy of the active mode.
2. *Multiple auto-term TF point* (MATFP): At these points, several modes are present; thus, auto-TFDs of several modes are non-zero as well as their cross-TFDs.* Therefore, STFD matrices

---

*It is theoretically possible to find TF points in which auto-TFDs of several signals are non-zeros, while their cross-TFDs are zero (Adel Belouchrani, personal communication). However, such points are not very probable [27].

of the modal coordinates, $\mathbf{D}_{\ddot{q}\ddot{q}}(t,f)$, have non-zero diagonal and off-diagonal elements. However, in most practical cases, only two modes may be present simultaneously in time and frequency; hence, $\mathbf{D}_{\ddot{q}\ddot{q}}(t,f)$ would be zero with only two non-zero diagonal and off-diagonal elements.

3. *Cross-term TF point* (*CTTFP*): At these points, the cross-TFDs of modal coordinates are non-zero, while their corresponding auto-TFDs are zero. Therefore, at such points, $\mathbf{D}_{\ddot{q}\ddot{q}}(t,f)$ matrices are off-diagonal with only two non-zero off-diagonal elements in most practical cases.

To illustrate the TF point classification described earlier, a synthetic example is presented, which is representative of typical data encountered in earthquake engineering. Consider a 3-DOF model with natural frequencies 0.50, 2.54, and 2.70 Hz. The two higher modes are specifically chosen to be closely spaced. Modal damping ratios are set at 5%, 1%, and 0.93%, for modes 1–3, respectively.

Figure 1 displays the real parts of SPWVD (auto-TFD and cross-TFD) of analytical modal coordinates under horizontal accelerogram recorded in El Centro Array #9 during Imperial Valley earthquake, 1940 [39], wherein all SPWVD values are colored in logarithmic scale. On the basis of
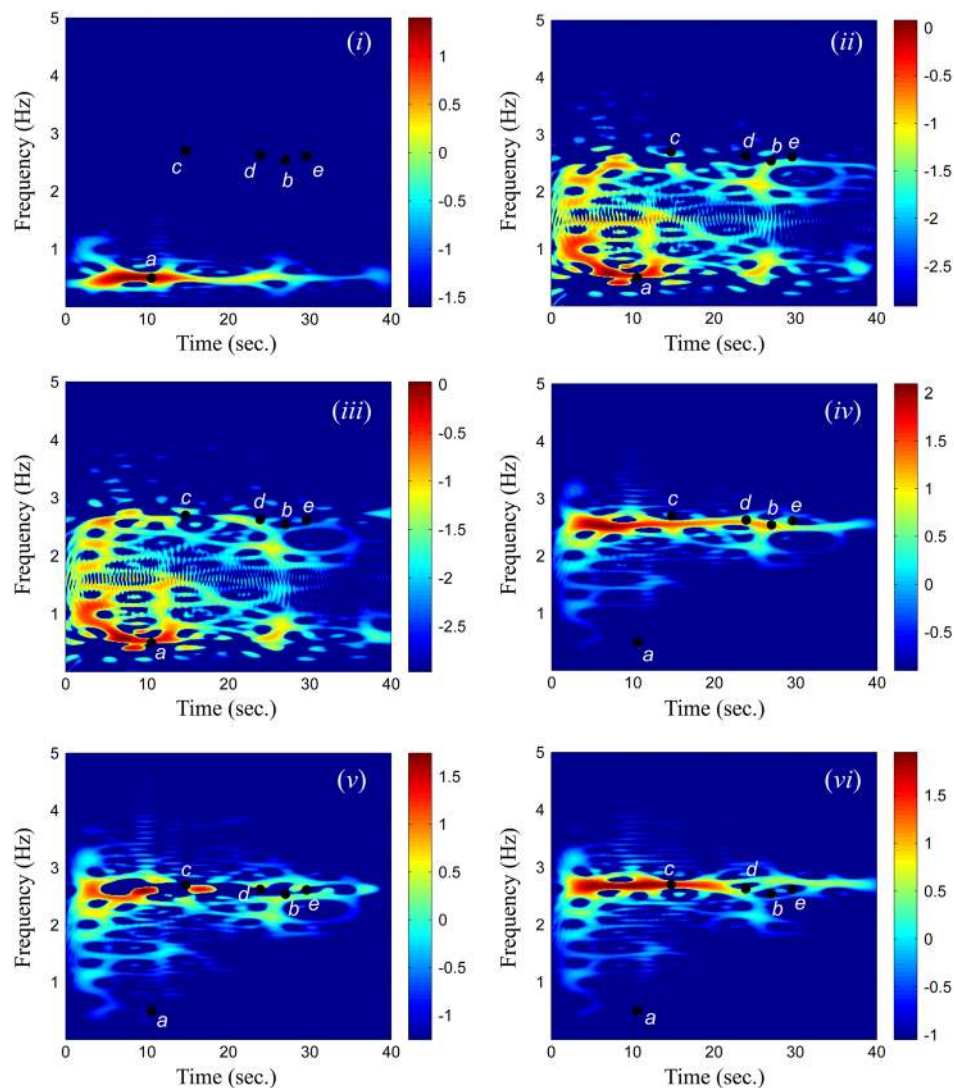

Figure 1. Auto-SPWVD and cross-SPWVD of analytical modal coordinates. (*i*) $D_{\ddot{q}_1\ddot{q}_1}$, (*ii*) $D_{\ddot{q}_1\ddot{q}_2}$, (*iii*) $D_{\ddot{q}_1\ddot{q}_3}$, (*iv*) $D_{\ddot{q}_2\ddot{q}_2}$, (*v*) $D_{\ddot{q}_2\ddot{q}_3}$, and (*vi*) $D_{\ddot{q}_3\ddot{q}_3}$.

the aforementioned definitions, examples for SATFPs, MATFPs, and CTTFPs are marked on this figure. To wit, points $a(t=10.55, f=0.50)$, $b(t=27.01, f=2.54)$, and $c(t=14.73, f=2.70)$ are SATFPs for the first, second, and third modes, respectively, and the STFD matrices at these points are

$$
\mathbf{D}_{\ddot{q}\ddot{q}}(a) = \begin{bmatrix} \underline{17.79} & 0.01+0.50i & 0.01+0.44i \\ 0.01-0.50i & -0.04 & -0.05+0.03i \\ 0.01-0.44i & -0.05-0.03i & -0.01 \end{bmatrix}
$$

$$
\mathbf{D}_{\ddot{q}\ddot{q}}(b) = \begin{bmatrix} 0.00 & -0.02+0.01i & -0.01 \\ -0.02-0.01i & \underline{16.50} & 0.16+0.63i \\ -0.01 & 0.16-0.63i & -0.55 \end{bmatrix}
$$

$$
\mathbf{D}_{\ddot{q}\ddot{q}}(c) = \begin{bmatrix} 0.00 & -0.01i & -0.01+0.04i \\ 0.01i & 0.24 & -0.41+3.05i \\ -0.01-0.04i & -0.41-3.05i & \underline{50.24} \end{bmatrix}
$$

Because the first mode is far from other modes in frequency domain—consequently, in TF domain—there is not an MATFP at which all three modes are present. On the other hand, there many MATFPs at which both the second and third modes are present simultaneously, because they are closely spaced modes in the frequency domain. Point $d(t=23.91, f=2.62)$, whose STFD matrix is shown later, can be labeled as an MATFP.

$$
\mathbf{D}_{\ddot{q}\ddot{q}}(d) = \begin{bmatrix} 0.00 & -0.05-0.01i & 0.01+0.01i \\ -0.05+0.01i & \underline{13.59} & \underline{-4.95+0.58i} \\ 0.01-0.01i & \underline{-4.95-0.58i} & \underline{1.82} \end{bmatrix}
$$

Also, because a TF distribution with minimum interference terms has been utilized in this example, there is no CTTFP between the first and second and or between the first and third modes. However, such points can be detected between the second and third modes, as they are close. Point $e(t=29.60, f=2.60)$ is an example CTTFP whose STFD matrix is

$$
\mathbf{D}_{\ddot{q}\ddot{q}}(e) = \begin{bmatrix} 0.00 & -0.01i & 0.00 \\ 0.01i & -0.41 & \underline{-1.89-0.89i} \\ 0.00 & \underline{-1.89+0.89i} & -0.23 \end{bmatrix}
$$

Considering the aforementioned definitions, at the SATFPs of the k-th mode, $\mathbf{D}_{\ddot{q}\ddot{q}}(t,f)$ is diagonal with only one non-zero diagonal element. Thus, Equation (4) can be converted to

$$
\mathbf{D}_{\ddot{x}'\ddot{x}'}(t_k, f_k) = \boldsymbol{\phi}_k D_{\ddot{q}_k \ddot{q}_k}(t_k, f_k) \boldsymbol{\phi}_k^{\ T} \tag{6}
$$

where $\boldsymbol{\phi}_k$ is the k-th column of $\boldsymbol{\phi}$, and $D_{\ddot{q}_k \ddot{q}_k}(t_k, f_k)$ is the k-th mode's auto-TFD. Equation (6) is arguably the most significant relationship in TF-based BSS problems as will be discussed later. Nevertheless, the detection of an SATFP is not easy, because the modal coordinates' STFD matrices

are not available. Hence, we use STFD matrices of the response signals instead to locate such points. In our previous study [11], the following criterion was used to that end

$$\left| \frac{\max_i |\lambda_i[\mathbf{D}_{\ddot{\mathbf{x}}'\ddot{\mathbf{x}}'}(t,f)]|}{\|\mathbf{D}_{\ddot{\mathbf{x}}'\ddot{\mathbf{x}}'}(t,f)\|_F} - 1 \right| < \epsilon \tag{7}$$

where ϵ is a small positive scalar, $\|.\|_F$ denotes the Frobenius norm, and $\max_i |\lambda_i[\mathbf{D}_{\ddot{\mathbf{x}}'\ddot{\mathbf{x}}'}(t,f)]|$ represents the largest eigenvalue of its argument matrix. This criterion can be used, because the STFD matrix of modal coordinates at each SATFP is of rank one or, in more precisely case of real data, has one eigenvalue that is significantly larger than the other values. The eigenvalues of the STFD matrix of the response signals can be used instead of their modal coordinate counterparts, when the mode shape matrix is unitary, which is not generally valid.[†] For this reason, a pre-whitening step is used to make the mixing matrix unitary [40]. However, for underdetermined cases—that is, the main subject of this study—the mode shape matrix is not unitary at all, so the proposed criterion can only be used as an approximation [25]. The criterion presented in Equation (7) has been calculated for points *a*, *b*, *c*, *d*, and *e* in Table I, where it may be observed the points *d* and *e* are incorrectly identified as SATFPs. To make improvements on the SATFP selection, Fevotte and Doncarli [40] have proposed the following criterion

$$\left| \frac{\max_i |\lambda_i[\mathbf{D}_{\ddot{\mathbf{x}}'\ddot{\mathbf{x}}'}(t,f)]|}{\sum_i |\lambda_i[\mathbf{D}_{\ddot{\mathbf{x}}'\ddot{\mathbf{x}}'}(t,f)]|} - 1 \right| < \epsilon \tag{8}$$

where ϵ is a very small number. Values of this criterion are also calculated and shown in Table I. As seen, this criterion yields a lower value for point *e* than other points, indicating better performance. Nevertheless, it is also unable to detect point *d* as an MATFP. Generally, for an STFD response matrix given below, it can be shown that Equation (8) also does not work well, especially when α and β values are close.[‡]

$$\mathbf{D}_{\ddot{\mathbf{x}}'\ddot{\mathbf{x}}'}(t,f) = \begin{bmatrix} 0 & 0 & 0 \\ 0 & \alpha & \beta \\ 0 & \beta & \alpha \end{bmatrix} \tag{9}$$

Although the proposed criterion in Equation (8) has better performance in deselecting CTTFPs, it is only applicable to problems for which the mixing matrix is unitary, similar to Equation (7). This problem can be circumvented by employing SVD instead of eigen-analysis as suggested by Giulieri *et al.* [41]. That is, TF points are selected so that the following index is 1

$$C(t,f) = \frac{\max_i \{\sigma_i[\mathbf{D}_{\ddot{\mathbf{x}}'\ddot{\mathbf{x}}'}(t,f)]\}}{\sum_i \{\sigma_i[\mathbf{D}_{\ddot{\mathbf{x}}'\ddot{\mathbf{x}}'}(t,f)]\}} \tag{10}$$

Table I. Values obtained from different SATFP selection criteria.

	a	*b*	*c*	*d*	*e*
$\frac{\max_i |\lambda_i[\mathbf{D}_{\ddot{\mathbf{x}}'\ddot{\mathbf{x}}'}(t,f)]|}{\|\mathbf{D}_{\ddot{\mathbf{x}}'\ddot{\mathbf{x}}'}(t,f)\|_F}$	1.0000	0.9994	1.0000	1.0000	0.8062
$\frac{\max_i |\lambda_i[\mathbf{D}_{\ddot{\mathbf{x}}'\ddot{\mathbf{x}}'}(t,f)]|}{\sum_i |\lambda_i[\mathbf{D}_{\ddot{\mathbf{x}}'\ddot{\mathbf{x}}'}(t,f)]|}$	0.9915	0.9665	0.9989	0.9983	0.5767
$\frac{\max_i \{\sigma_i[\mathbf{D}_{\ddot{\mathbf{x}}'\ddot{\mathbf{x}}'}(t,f)]\}}{\sum_i \{\sigma_i[\mathbf{D}_{\ddot{\mathbf{x}}'\ddot{\mathbf{x}}'}(t,f)]\}}$	0.9915	0.9665	0.9989	0.9983	0.5767

[†]For structural systems for which the mass matrix is diagonal with identical elements, the mode shape matrix can be assumed to be unitary.
[‡]For cases with $\alpha = \beta$, both this new criterion and Equation (7) are no longer able to identify point *d* as an MATFP.

where $\sigma_i[.]$ denotes the singular value of its argument matrix. This new criterion is also calculated for points a, b, c, d, and e, which yielded identical values to those obtained from Equation (8) (cf. Table I) without assuming a unitary mode shape matrix. Also, note that this new criterion cannot yet properly detect MATFPs.

As mentioned, for purely disjoint modes, the aforementioned metric is theoretically 1 at SATFPs. However, in practice, the local maximum of $C(t,f)$ over the TF plane can be used. In the present study, to find local maxima of such a function, the following criteria is used [40]

$$\|\mathrm{Grad}_C(t,f)\| < \epsilon_{\mathrm{Grad}} \tag{11}$$

$$\mathbf{H}_C(t,f) < 0 \tag{12}$$

where $\mathrm{Grad}_C(t,f)$ and $\mathbf{H}_C(t,f)$ denote the gradient function and the Hessian matrix of $C(t,f)$, respectively. ϵ_{Grad} in Equation (11) is chosen to be very small in order to select points around the local maxima. To prevent selecting points with nearly zero energy, $C(t,f)$ must be calculated for points satisfying the following condition

$$\frac{\sum_i \{\sigma_i[\mathbf{D}_{\ddot{x}'\ddot{x}'}(t,f)]\}}{\overline{\sigma}} > \epsilon_{\mathrm{Energy}} \tag{13}$$

where

$$\overline{\sigma} = \frac{1}{n_f n_t} \sum_{t,f} \sum_{i=1}^{i=n} \sigma_i[\mathbf{D}_{\ddot{x}'\ddot{x}'}(t,f)] \tag{14}$$

where n_f and n_t are the number of frequency and time points, respectively, in which $\sigma_i[\mathbf{D}_{\ddot{x}'\ddot{x}'}(t,f)]$ is calculated. Also, $\epsilon_{\mathrm{Energy}}$ is very small and chosen experimentally (typically a value of 1% will work).

2.2. Estimation of the mode shapes

By selecting SATFPs, we have TF points at which the modes are purely disjoint. Suppose that there are two SATFPs (t_1,f_1) and (t_2,f_2) that are related to k-th mode. Thanks to Equation (6), the following relationships can be written

$$\mathbf{D}_{\ddot{x}'\ddot{x}'}(t_1,f_1) = \boldsymbol{\phi}_k D_{\ddot{q}_k\ddot{q}_k}(t_1,f_1)\boldsymbol{\phi}_k^T \tag{15}$$

$$\mathbf{D}_{\ddot{x}'\ddot{x}'}(t_2,f_2) = \boldsymbol{\phi}_k D_{\ddot{q}_k\ddot{q}_k}(t_2,f_2)\boldsymbol{\phi}_k^T \tag{16}$$

As seen, $\mathbf{D}_{\ddot{x}'\ddot{x}'}(t_1,f_1)$ and $\mathbf{D}_{\ddot{x}'\ddot{x}'}(t_2,f_2)$ have the same eigenvectors (corresponding to the largest eigenvalue); that is, the STFD matrices of response signals at all SATFPs corresponding to the same mode have the same eigenvector [25]. Therefore, a clustering approach (see, for example, [42] for clustering techniques) can be used to categorize the principal eigenvectors of the STFD matrices of response signals at all SATFPs into m (number of total active modes) groups. Note that this clustering approach can only be applicable if the mode shape vectors are *pairwise linearly independent*—that is, $\boldsymbol{\phi}_i \neq \alpha\boldsymbol{\phi}_j \forall i,j = 1, \ldots, m$. Such independence is fully satisfied for determinate or overdetermined cases; however, it must be carefully considered for underdetermined problems. Note that, if the earthquake excitation has a very narrow-band frequency content, and its dominant frequency falls within two modes, then the method is unable to find the mode shapes of these modes, because no SATFPs of such modes are detected. However, this hypothetical situation is arguably extremely rare. At least, the authors have yet to observe such a scenario with real-life data. On the basis of this assumption, k-means

clustering is used in the present study. This clustering is a partitioning method through which data (here, a set of eigenvectors) are grouped into k mutually exclusive clusters. To do so, a distance measure is used by which k-means partitions the eigenvectors into clusters in which the vectors within each cluster are as close to each other as possible and as far from those vectors that belong to other clusters as possible. Herein, the standard modal assurance criterion (MAC) is used as a distance measure, which is calculated through

$$\text{MAC}_{ij} = \frac{(\boldsymbol{\phi}_i \cdot \boldsymbol{\phi}_j)^2}{\|\boldsymbol{\phi}_i\|^2 \|\boldsymbol{\phi}_j\|^2} \tag{17}$$

k-means starts with k assumed eigenvectors as true mode shapes; then, by assuming them as clusters' centroids, other eigenvectors are clustered so that the sum of their distances (i.e., MAC) from the cluster centroid is minimized for all clusters. There are several methods to produce the initial estimation of the centroids. In the present study, k (the number of assumed clusters) points are uniformly selected at random from the data. After the initial estimation of the clusters' centroids, k-means algorithm tries to find the centroid and also move vectors between clusters until the sum of distances cannot be decreased further.

One of the important parameters in the clustering approach is the number of clusters. Theoretically, if all selected points are exactly SATFPs, then the number of clusters is the number of contributing modes. However, the number of active modes cannot be accurately estimated blindly. Moreover, selected points are not usually pure SATFPs because of modal frequency overlapping between the closely spaced modes, especially for higher level of damping. One solution for this problem is to repeat the clustering procedure for a range of number of clusters (usually greater than the number of expected contributing modes). After that, a *silhouette* [43] *diagram* can be used to find the best number of clusters. This diagram provides a succinct graphical representation of how well each object lies within its cluster [44]. The silhouette index for the l-th datum (here, eigenvector) is calculated through

$$s_l = \frac{b_l - a_l}{\max\{a_l, \ b_l\}} \tag{18}$$

where a_l is the average of dissimilarity (here, $1 - \text{MAC}_{lr}$) between the l-th datum with all other data within the same cluster and b_l is the lowest average dissimilarity between the l-th datum with other clusters. To calculate b_l, the average dissimilarity of this datum with all the data of another single cluster is calculated. Then, this calculation is repeated for every cluster where the l-th datum is not a member. b_l is the minimum among all these averages. Considering Equation (18), s_l varies between -1 and $+1$. An s_l value close to 1 denotes that the datum is appropriately clustered, while a value close to -1 means it would be more appropriate if this datum was clustered in its neighboring cluster. A zero s_l value indicates that the datum is located on the border of two clusters. As an illustration, Figure 2
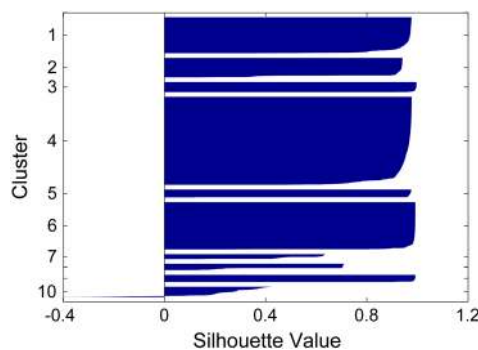

Figure 2. A silhouette diagram with 10 clusters.

displays a silhouette diagram for which the number of clusters is assumed to be 10. The number of members of each cluster depicts the number of eigenvectors that are similar to each other. For example, this figure shows that the fourth cluster has a larger size, because a large number of the selected SATFPs are related to a specific mode. Note that the order of appearance of clusters along the y-axis is random, while the order of appearance of members of a cluster is descending with the similarity between the member and the centroid of the cluster. On the basis of the silhouette definition, the best choice for the number of clusters yields the best clustering, which produces the maximum value of the silhouette average, that is,

$$\overline{S} = \frac{1}{k} \sum_{i=1}^{k} \overline{s}_i, \tag{19}$$

$$\overline{s}_i = \frac{1}{M_i} \sum_{j=1}^{M_i} s_j^i, \tag{20}$$

where s_j^i is the silhouette index for the j-th datum placed in the i-th cluster and M_i denotes the number of the i-th cluster's members. Further details on the clustering process are deferred to the verification problem presented in Section 3.

2.3. Recovering the modal coordinates' time–frequency domains

A subspace-based method that was proposed in [28] is described herein, through which the modal coordinates' TFDs can be recovered at all TF points regardless of their type (SATFPs, MATFPs, or CTTFPs).

Assume that there exists a point $(t' f')$ at which p modes are present where $p < m$. In what follows, an attempt is made to determine which p modes are present, as well as their energy contributions.

If these p modes are labeled with $\alpha_1, \alpha_2, ..., \alpha_p$ indices, then Equation (4) can be rewritten at this TF point as

$$\mathbf{D}_{\ddot{x}'\ddot{x}'}(t', f') = \widetilde{\boldsymbol{\phi}} \mathbf{D}_{\ddot{\tilde{q}}\ddot{\tilde{q}}}(t', f') \widetilde{\boldsymbol{\phi}}^T \tag{21}$$

where

$$\widetilde{\boldsymbol{\phi}} = \left[\boldsymbol{\phi}_{\alpha_1}, ..., \boldsymbol{\phi}_{\alpha_p}\right] \tag{22}$$

$$\widetilde{\ddot{q}} = \left[\ddot{\tilde{q}}_{\alpha_1}(t), ..., \ddot{\tilde{q}}_{\alpha_p}(t)\right]^T \tag{23}$$

As the matrix $\mathbf{D}_{\ddot{\tilde{q}}\ddot{\tilde{q}}}(t', f')$ is full rank, a projector onto the orthogonal compliment of $\mathbf{D}_{\ddot{x}'\ddot{x}'}(t' f')$ can be defined as

$$\mathbf{P} = \mathbf{I} - \mathbf{V}\mathbf{V}^T \tag{24}$$

where $\mathbf{I}$ is an $n \times n$ identity matrix and $\mathbf{V}$ is an $n \times p$ matrix formed by the p principal singular vectors of $\mathbf{D}_{\ddot{x}'\ddot{x}'}(t', f')$. It can be shown that [28]

$$\mathbf{P}\boldsymbol{\phi}_i = \mathbf{0} \quad \forall \quad i \in \left\{\alpha_1, , \alpha_2, ..., \alpha_p\right\} \tag{25}$$

$$\mathbf{P}\boldsymbol{\phi}_i \neq \mathbf{0} \quad \forall \quad i \notin \left\{\alpha_1, , \alpha_2, ..., \alpha_p\right\} \tag{26}$$

Thus, by considering noise effects and calculation errors, $\{\alpha_1, \alpha_2, ..., \alpha_p\}$ can be obtained as the p modes that have the smallest $\|\mathbf{P}\boldsymbol{\phi}_i\|$. This process can be employed at all TF points (with sufficient energy) to detect their present modes. Note that for employing the proposed subspace approach,

mode shape vectors must have unit lengths. Then, the modal coordinates' TFDs can be easily re-covered as the diagonal elements of the following matrix

$$\mathbf{D}_{\tilde{q}\tilde{q}}(t',f') = \widetilde{\boldsymbol{\phi}}^{\,\#}\mathbf{D}_{\ddot{x}'\ddot{x}'}(t',f')\widetilde{\boldsymbol{\phi}}^{\,\#^T} \tag{27}$$

where # denotes the Moore–Penrose pseudo-inversion operator.

Remark 1
Estimation of the *number* of present sources at each TF point is a challenging problem in electrical engineering literature [28]; however, for civil engineering applications, $p = 2$ and $p = 3$ for 2D and 3D problems, respectively, are reasonable assumptions.

Remark 2
The aforementioned approach works well provided that the number of present modes at each TF point is less than the number of recorded response signals. Considering Remark , at least three and four sensors must be used for identification of 2D and 3D problems, respectively.

To show how the proposed approach works, let us consider again the 3-DOF system of Section 2.1. The mode shape matrix for this system is

$$\boldsymbol{\phi} = \begin{bmatrix} 0.059 & -0.704 & -0.708 \\ 0.677 & -0.493 & 0.546 \\ 0.734 & 0.512 & -0.447 \end{bmatrix} \tag{28}$$

$\|\mathbf{P}\boldsymbol{\phi}_i\|$ for these points are shown in Table II. As mentioned earlier, two smallest values indicate two modes that may be present at a point. Two modes that present such a circumstance are introduced in Table II. For both MATFPs and CTTFPs, the criterion of selecting the modes with two smallest $\|\mathbf{P}\boldsymbol{\phi}_i\|$ works well. However, for SATFPs, it is important to exclude the modes that are not actually present. For this reason, the ratio between two smallest $\|\mathbf{P}\boldsymbol{\phi}_i\|$ is used in this study to decide whether a TF point is an SATFP or not. This index is calculated for selected points and is shown in Table II. As seen, for SATFPs (i.e., points *a*, *b*, and *c*), this index is small, whereas for points *d* and *e*, it is large. As such, it appears that a threshold value of 0.1 can be used to detect SATFPs. Present modes detected by this threshold are shown in Table II as well as their recovered auto-TFDs by Equation (27). As seen, recovered TFDs are identical to corresponding diagonal values of matrices $\mathbf{D}_{\ddot{q}\ddot{q}}(a)$, $\mathbf{D}_{\ddot{q}\ddot{q}}(b)$, $\mathbf{D}_{\ddot{q}\ddot{q}}(c)$, $\mathbf{D}_{\ddot{q}\ddot{q}}(d)$, and $\mathbf{D}_{\ddot{q}\ddot{q}}(e)$.

2.3.1. Natural frequency identification. Having TFD of a mode at all TF points, natural frequency of the mode can be detected through three approaches: (i) synthesizing time signals of modal coordinates

Table II. Values of $\|\mathbf{P}\boldsymbol{\phi}_i\|$ for selected points.

	$\|\mathbf{P}\boldsymbol{\phi}_1\|$	$\|\mathbf{P}\boldsymbol{\phi}_2\|$	$\|\mathbf{P}\boldsymbol{\phi}_3\|$	Two modes with smallest $\|\mathbf{P}\boldsymbol{\phi}_i\|$	Ratio	Present modes	Recovered $D_{\ddot{q}_i\ddot{q}_i}(t,f)$
a	0.0089	0.6298	0.7767	1, 2	0.01	1	17.79
b	0.9999	0.0010	0.0164	2, 3	0.06	2	16.50
c	0.9749	0.2221	0.0141	2, 3	0.06	3	50.25
d	0.7072	0.2419	0.6643	2, 3	0.36	2, 3	13.59, 1.82
e	1.0000	0.0014	0.0070	2, 3	0.2	2, 3	−0.41, −0.23

through inverse TF transform and concurrent analysis of them as suggested in [11]; (ii) identifying natural frequency as frequency point with highest energy concentration in whole TF plane; and (iii) identifying natural frequency as frequency line with highest energy concentration. The first method is not favorable, as inverse TF transform is an arduous task for RID family [25]. The second method is simple and applicable; however, it may result in spurious frequencies if input motion has a dominant frequency with a high level of energy concentration at a short time window. The third method circumvents this problem, as its energy concentration throughout the entire time window is used. For this purpose, an index is introduced as

$$E(f) = \frac{\int_{-\infty}^{+\infty} TFD(t,f)dt}{\iint_{-\infty}^{+\infty} TFD(t,f)dt\,df} \tag{29}$$

which is the ratio of time-marginal energy of a signal at a specific frequency to the total energy. It is expected that this index would be at a maximum at the natural frequency of the mode, because the maximum time average of energy concentration occurs at this frequency.

2.3.2. Damping ratio identification. There are several methods for identifying damping ratios from free vibration signals [45–47]. On the other hand, estimation of damping ratios from response signals recorded during strong ground shaking is a challenging problem, even when the input excitations are measured. In a previous study [11], we used cross-relations among the extracted modal coordinates for identification of both the natural frequencies and the damping ratios. That approach is not applicable to the current scenario, because it was only valid for systems subject to a single input and also because the time signals of the modal coordinates are not available here.

It is well known that earthquake input motions are non-stationary signals—their frequency content varies with time. Thus, at certain instants, certain modes may be excited, while others are at rest. Hence, the damping ratios of the at-rest modes can be identified through the free vibration portions of their TFDs. Free vibration of the *i*-th modal coordinate in time domain is

$$q_i(t) = \alpha_i e^{-\xi_i \omega_{ni} t} \sin(\omega_{di} t + \theta_i) \tag{30}$$

where α_i and θ_i are two constants to be determined from initial conditions; ξ_i is the damping ratio; and $\omega_{ni} = 2\pi f_{ni}$ and $\omega_{di} = \omega_{ni}\sqrt{1 - \xi_i^2}$ are respectively the undamped and damped natural frequencies in rad/s, with f_{ni} denoting the undamped natural frequency in Hertz. For simplicity, first, consider the continuous WVD of this signals, which is given by

$$\text{WVD}_{q_i q_i}(t,f) = \int_{-\infty}^{+\infty} \hat{q}_i\left(t + \frac{\tau}{2}\right) \hat{q}_i^*\left(t - \frac{\tau}{2}\right) e^{-j2\pi f\tau} d\tau \tag{31}$$

where $\hat{q}_i(t) = q_i(t) + j H[q_i(t)]$ is the analytic associate of the signal $q_i(t)$, in which $H[\bullet]$ denotes a Hilbert transform. The Hilbert transform of a signal $q_i(t)$ is given by

$$H[q_i(t)] = \frac{1}{\pi}\int_{-\infty}^{+\infty} \frac{q_i(\tau)}{t - \tau} d\tau. \tag{32}$$

For small values of the damping ratio, $H[q_i(t)]$ is approximately equal to [48]

$$H[q_i(t)] \approx -\alpha_i e^{-\xi_i \omega_{ni} t} \cos(\omega_{di} t + \theta_i) \tag{33}$$

By inserting Equations (32) and (33) into Equation (31), the continuous auto-TFD of the i-th modal coordinate's free vibration can be simplified as

$$\text{WVD}_{q_i q_i}(t, f_{ni}) = \alpha_i^2 e^{-2\xi_i \omega_{ni} t} \, F\left[e^{-j\omega_{di} t}\right]_{f=f_{ni}} \tag{34}$$

where $F[\bullet]_{f_{ni}}$ denotes a Fourier transform at the natural frequency f_{ni}. Noting that $\text{WVD}_{q_i q_i}(t, f_{ni})$ is an exponential time signal whose decay rate is $2\xi_i \omega_{ni}$, the damping ratio can be easily detected through a simple curve fitting. To extend this equation to the SPWVD, which is used in the present study, the following expression can be used [36]

$$\text{SPWVD}_{q_i q_i}(t, f) = g_1(t) * \text{WVD}_{q_i q_i}(t, f) * G_2(f) \tag{35}$$

where $g_1(t)$ and $G_2(f)$ are the time and frequency smoothing windows, respectively, and $*$ is the convolution operator. At the frequency that corresponds to the natural frequency of the i-th mode, $G_2(f)$ is a constant. Therefore, by applying, for example, a *Hamming* window for $g_1(t)$, the SPWVD of the free vibration modal coordinate signal can be expressed as

$$\text{SPWVD}_{q_i q_i}(t, f_{ni}) = \left[0.54 - 0.46\cos\left(\frac{2\pi t}{L-1}\right)\right] * \alpha_i^2 e^{-2\xi_i \omega_{ni} t} \, F\left[e^{-j\omega_{di} t}\right]_{f=f_{ni}} \tag{36}$$

in which L is the time length of the window. By calculating the convolution, the SPWVD can be expressed as

$$\text{SPWVD}_{q_i q_i}(t, f_{ni}) = A e^{-2\xi_i \omega_{ni} t} \tag{37}$$

where

$$A = \alpha_i^2 e^{-2\xi_i \omega_{ni} L} \frac{\left(2.66 + 0.5\xi_i^2 \omega_{ni}^2 L^2\right)\left(e^{2\xi_i \omega_{ni} L} - 1\right)}{\xi_i \omega_{ni}\left(\pi^2 + \xi_i^2 \omega_{ni}^2 L^2\right)} \, F\left[e^{-j\omega_{di} t}\right]_{f=f_{ni}} \tag{38}$$

Equation (38) shows that $\text{SPWVD}_{q_i q_i}(t, f_{ni})$ is also an exponential time signal whose decay rate is $2\xi_i \omega_{ni}$.

To examine the proposed approach, consider, for example, a modal coordinate's free vibration signal with $f_n = 2$ Hz and $\xi = 5\%$. The time history of this signal and its SPWVD at $f = 2$ Hz are shown in Figure 3(a). In this figure, the starting time of the signal and the time at which its SPWVD peaks are shown by t_0 and t_p, respectively. To calculate the SPWVD, a Hamming window with $L = 3$ s is used. Note that the peak time is bounded as

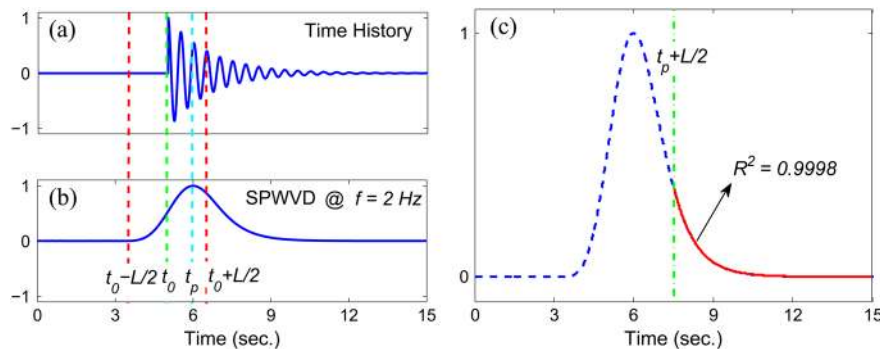$$t_0 - \frac{L}{2} \leq t_p \leq t_0 + \frac{L}{2} \tag{39}$$

Figure 3. Damping estimation from SPWVD of free vibration signal. (a) Time history, (b) SPWVD at natural frequency, and (c) fitting process.

In real-life situations, the time history of the free vibration signal is not available, so we have to select a suitable portion of the TFD within which Equation (37) is valid, without knowing t_0. To make sure that the selected initial point is greater than t_0, we suggest to select $t = t_p + L/2$ so that

$$t_0 \leq t = t_p + \frac{L}{2} \tag{40}$$

The last point of the fitting curve can be easily selected as the last point with positive energy and negative derivative, or as the point through which the best fit (i.e., the smallest residual) is obtained, provided that we have a reasonable data length—for example, 10 cycles of vibration. For the example shown in Figure 3(a), the fitting curve is presented in Figure 3(b). As this figure indicates, curve fitting is nearly perfect ($\xi = 4.98\%$) and the goodness-of-fit, R^2, is very close to 1 (the ideal case).

$$R^2 = \frac{\sum_{i=1}^{n}(\hat{y}_i - \overline{y})^2}{\sum_{i=1}^{n}(y_i - \overline{y})^2} \tag{41}$$

where y_i, $\hat{y}_i$, and $\overline{y}$ are the i-th exact and fitted values, and the average of n exact values used for fitting, respectively.

Remark 3
To the best of the authors' knowledge, the only way to distinguish between the free vibrations and the reduced excitation portions of the recovered TFD of the mode is to check whether this portion follows an exponentially decaying function introduced in Equation (37).

2.3.3. Summary. In order to make the implementation of the proposed identification method easy for the readers, all of the necessary steps are summarized here:

Step 1: Compute the STFD matrices of absolute acceleration response signals via Equation (5) using their analytic forms.
Step 2: Locate TF points with non-zero energy via Equations (13) and (14) with suitable ϵ_{Energy}.
Step 3: Select the SATFPs via Equations (10)–(12) with $\epsilon_{Grad} = 0.1\%$.
Step 4: Perform the *k*-means clustering of the principal eigenvectors of the response signals' STFD matrices at selected SATFPs for a range of number of clusters.
Step 5: Calculate the average of silhouette values, $\overline{S}$, using Equations (18)–(20) over all clustered data, for all iterations.
Step 6: Determine the best number of clusters, which corresponds to maximum $\overline{S}$.
Step 7: Calculate the MAC indices (cf. Equation (17)) among the recovered mode shapes—that is, at the centroids of clusters—and select the 'true mode shapes' as those with the highest $\overline{s}_i$.
Step 8: Determine the modes that are present at each TF point by using Equations (24)–(26).
Step 9: Recover the modal coordinates' TFDs by using Equation (27).
Step 10: Compute the natural frequencies and damping ratios for each recovered modal coordinate's TFD via Equations (29), (37), (38), and (40).

Note that the primary assumptions adopted for the aforementioned algorithm are as follows: (i) there are at least three and four sensors for 2D and 3D problems, respectively, and (ii) the mode shape vectors are pairwise linearly independent. The accuracy of results will deteriorate if these conditions are not met.

3. VERIFICATION AND PERFORMANCE EVALUATION OF THE PROPOSED METHOD

The performance of the proposed identification approach is explored here by using synthetic data from a 10-story shear-building model. We have used the same model in a previous study to verify a modal identification method for data from underdetermined free/ambient vibration surveys [49]. Its stories have identical floor mass and interstory stiffness values, given respectively as 100 mt and 176.729 MN/m. Mass proportional damping is considered, with the first mode's damping ratio set at 5% of critical. Table III displays the resulting natural frequencies and damping ratios of this synthetic model.

The horizontal accelerogram recorded by the El Centro Array #9 during the 1940 Imperial Valley earthquake [39] is used as input motion of the system. The dynamic analysis was carried out using

Table III. Natural frequencies and damping ratios of the 10-story model.

Mode No.	1	2	3	4	5	6	7	8	9	10
f_n(Hz)	1.00	2.98	4.89	6.69	8.34	9.81	11.06	12.07	12.79	13.23
ξ(%)	5.00	1.68	1.02	0.75	0.60	0.51	0.45	0.41	0.39	0.38

the lsim command in MATLAB [50] with a 100-Hz sampling frequency. Figure 4 displays the TF representations of the first floor and the roof absolute acceleration responses using SPWVD.

3.1. Complete instrumentation

First, complete instrumentation is considered to examine the performance of the proposed method for determinate problems. Figure 5(a) displays automatically selected auto-source points with $\epsilon_{\text{Grad}} = 0.001$ and $\epsilon_{\text{Energy}} = 0$. Many frequency lines can be observed in this figure, and some of them are highly discontinuous in time. It is expected that those points that make up the highly discontinuous frequency lines to be SATFPs; however, it is probable that some MATFPs are among them, especially when two close modes have exactly the same energy. As will be shown later, it is possible to detect such points by post-processing the recovered modal coordinates' TFDs.

By employing the k-means clustering procedure, the estimated mode shapes are divided into k clusters. As mentioned earlier, it is recommended to repeat the clustering procedure for a range of values of k, to determine the most suitable number of clusters for which $\overline{S}$ is the largest. Also, to improve the accuracy of the proposed approach and also increase the computational speed, it is more desirable to cluster the same amount of data for each frequency bin, because k-means clustering suffers from difference between the densities of available data for each mode [51]. That is, the highest modes may be grouped with wrong clusters, because they usually have the lowest number of selected SATFPs. Here, we select the eigenvectors of 10 randomly selected SATFPs for each frequency bin. Figure 6
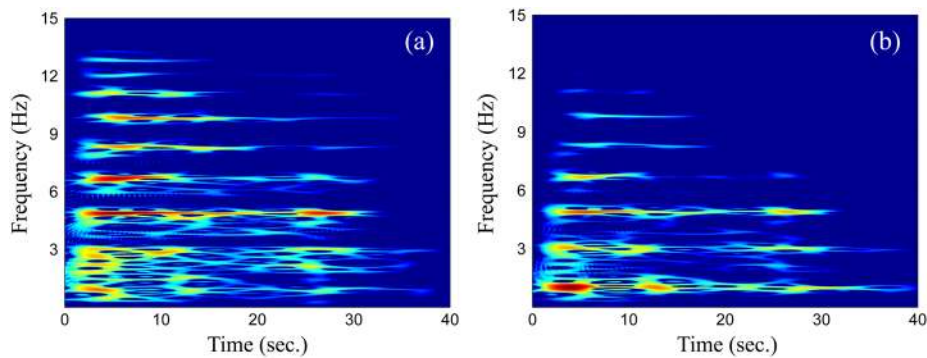

Figure 4. Time–frequency representations of (a) the first story and (b) roof responses.
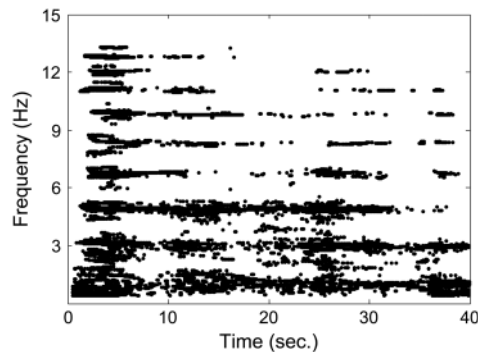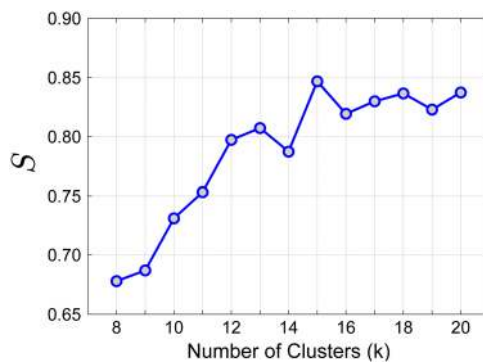

Figure 5. Selected auto-source points.

Figure 6. Variation of $\overline{S}$ with number of clusters.

displays the variation of $\overline{S}$ for a range of number of k values, where it is observed that the largest value of $\overline{S}$ is attained with $k = 15$. The silhouette diagram for that case is shown in Figure 7.

After determining the number of clusters, the cluster centroids are taken as the representative of mode shapes. However, it is important to extract the real clusters that represent the mode shapes, as in most cases—including the current example—the number of clusters is greater than the number of active modes. That is, some mode shapes are reduplicative or correspond to the mistakenly selected MATFPs. To distinguish such mode shapes, the MAC indices among all of the extracted mode shapes are calculated and are shown in Figure 8. As seen, clusters 1, 11; 3, 14; 5, 6; 8, 12; and 13, 15 are similar. Between two similar clusters, the cluster with greater $\overline{s}_i$ value is chosen as the final answer. Table IV presents the selected clusters, the silhouette average $\overline{s}_i$, the standard deviation of their silhouette values, and their corresponding mode numbers. The MAC indices between these identified mode shapes and
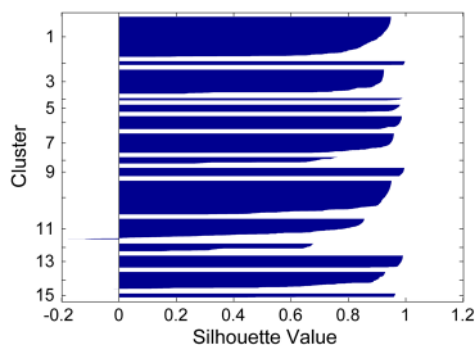

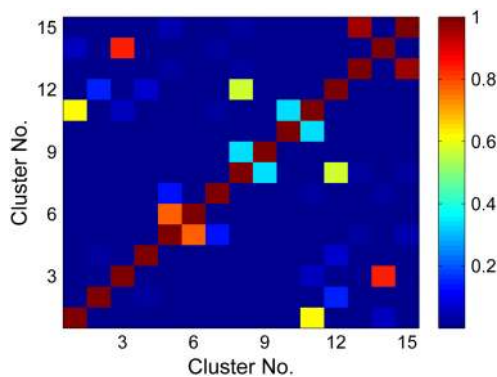Figure 7. Silhouette diagram with 15 clusters.

Figure 8. MAC among extracted mode shapes.

Table IV. Summary of mode shape identification results.

Mode no.	1	2	3	4	5	6	7	8	9	10
Cluster no.	10	1	3	7	6	13	9	12	2	4
First iteration										
$\bar{s}_i$	0.869	0.869	0.851	0.911	0.970	0.979	0.989	0.527	0.994	0.975
STDEV	0.136	0.116	0.155	0.071	0.021	0.018	0.005	0.186	0.007	0.015
MAC	0.998	0.985	0.994	0.999	0.997	0.996	1.000	0.824	0.999	0.965
Second iteration										
$\bar{s}_i$	0.931	0.926	0.913	0.948	0.981	0.986	0.993	0.664	0.995	0.983
STDEV	0.017	0.022	0.014	0.012	0.004	0.003	0.002	0.011	0.001	0.004
MAC	0.979	0.973	0.991	1.000	1.000	0.997	0.999	0.996	0.998	0.980

their exact counterparts are also shown in Table IV. As it can be observed from this table, except for mode 8, all of the identified clusters have high MAC values with respect to their corresponding exact mode shapes and high average silhouette values, which indicates that the mode shape identification step has been successful. Although the obtained results are satisfactory, it is possible to improve the accuracy of estimated mode shapes by removing data with low silhouette values, for example, $s_j^i < \bar{s}_i$, and by recalculating the centroids with the remaining vectors in each cluster. The new results are shown in Table IV as the 'Second iteration' results. As seen, removal of data with low silhouette values has considerably improved the MAC value for mode 8 whose $\bar{s}_i$ was low, while there were no significant changes for the other modes.

Figure 9 displays the identified mode shapes through the first and second iterations by red and green solid lines, respectively. In this figure, the clustered and exact mode shapes are also shown by gray and black solid lines, respectively. This figure clearly indicates that the identified shape for mode 8 has been significantly improved by removing those data that had the low silhouette values.

After finding the mode shapes, the modal coordinates' TFDs are recovered through the proposed subspace-based identification method. However, it is favorable to apply this method first on the selected points that were used during the mode shape estimation phase—that is, points shown in Figure 5. It is expected that all points will be classified as SATFP; however, because of errors in the proposed selection criterion—that is, Equation (10)—some MATFPs and rarely CTTFPs may have been included. Figure 10 displays the classification results, which are obtained using the same approach used in Table II. As seen, the subspace method is able to detect those TF points that are between the frequency lines (natural frequencies) as non-SATFPs. After removing them from the selected points, it is possible to repeat the mode shape identification step and the clustering phase to obtain more accurate results. This second iteration is not applied here, because the identified mode shapes are already very accurate.

By employing the subspace-based method along with Equation (27), the auto-TFDs of modal coordinates are recovered. As an illustration, the recovered modal coordinates for modes 2 and 8 are presented in which exact counterparts are also shown in Figure 11 side by side. As seen, the recovered
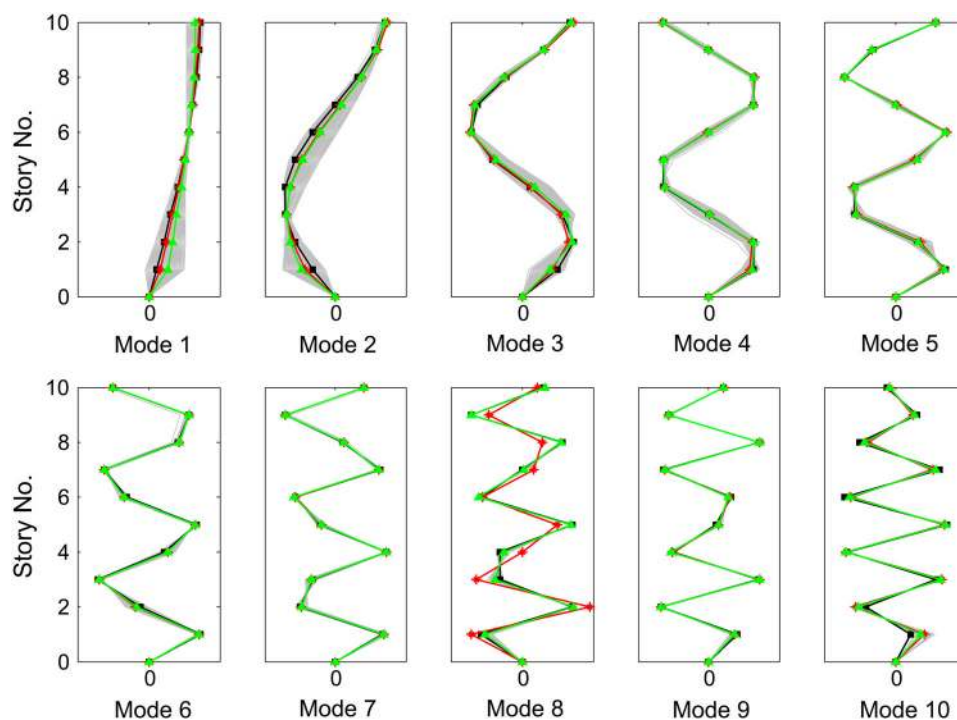

Figure 9. Clustered (gray), exact (black), first iteration (red), and second iteration (green) mode shapes.
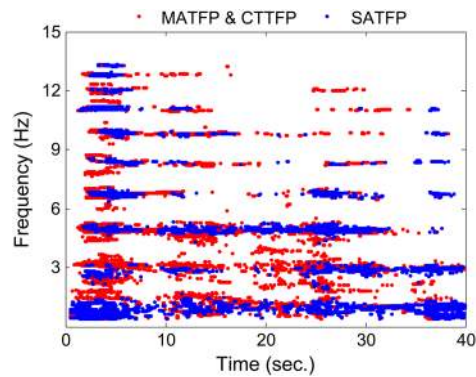
Figure 10. Classified selected points as SATFPs and MATFPs or CTTFPs.
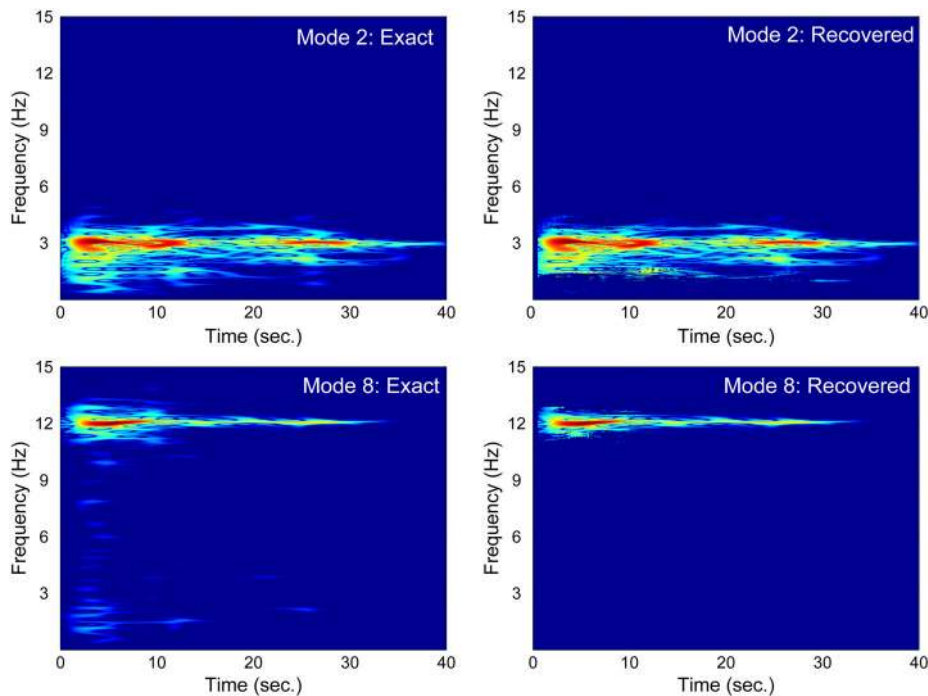

Figure 11. Comparison between the auto-TFDs of the exact and the recovered modal coordinates.

modal coordinates' TFDs are identical to their exact counterparts. Similar results were obtained for the other modes and are omitted here for brevity.

The natural frequency of each mode is calculated using the $E(f)$ index, which is shown as an example in Figure 12 for the sixth mode. The frequency corresponding to the maximum energy depicts that natural frequency of the mode. By calculating this index for all recovered modal coordinates, the natural frequencies (f_i) of all modes are identified as shown in Table V. To make the comparison easy, their analytical counterparts (f_e)—previously reported in Table III—and the identification errors are also shown in Table V. As seen, all of the natural frequencies are identified with less than 4% error. For this synthetic example, we anticipated that the damping ratios would be identified with high accuracy. Table V displays that the proposed method is successful in estimating damping ratios with errors less than 4% for modes 2–10. However, that first mode's damping ratio has not been detected accurately, because it has the lowest natural frequency, and as such, only a few free vibration cycles were available in the signals. For real-life cases, this should not a problem, because it is possible to continue recording response signals for a long window of time. Note that as it was mentioned in Remark , we selected the free vibration portion as the decaying part, which follows an exponentially decaying function with start and end times previously introduced.
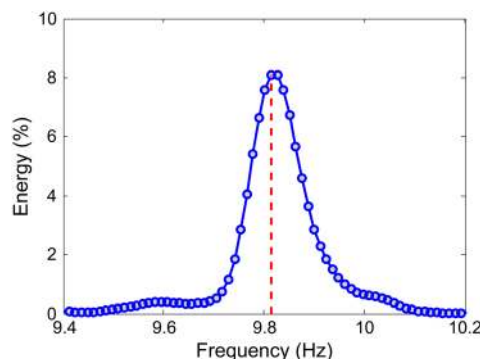
Figure 12. Variation of $E(f)$ for the sixth mode in the first iteration.

Table V. Identified and exact natural frequencies and damping ratios of the 10-story model.

Mode no.	1	2	3	4	5	6	7	8	9	10
f_i(Hz)	1.04	3.06	4.91	6.74	8.36	9.81	11.05	12.05	12.81	13.26
f_e(Hz)	1.00	2.98	4.89	6.69	8.34	9.81	11.06	12.07	12.79	13.23
$err(\%) = |f_e - f_i|/f_e$	4.00	2.68	0.41	0.75	0.24	0.00	0.09	0.17	0.16	0.23
$\xi_i(\%)$	6.12	1.62	0.98	0.72	0.59	0.51	0.45	0.40	0.38	0.37
$\xi_e(\%)$	5.00	1.68	1.02	0.75	0.60	0.51	0.45	0.41	0.39	0.38
$err(\%) = |\xi_e - \xi_i|/\xi_e$	22.40	3.57	3.92	4.00	1.67	0.00	0.00	2.44	2.56	2.63

3.2. Incomplete instrumentation

Herein, we make an attempt to reduce the number of sensors without losing any modes. For this, the sensors distribution must be carefully selected for a given number of sensors. As an example, we use five sensors to identify all 10 modes. As the proposed mode shape identification technique is based on the linear independence of the mode shapes, we try to a select sensor distribution scenario that results in a set of estimated mode shapes so that the maximum value of the MAC indices among them is a minimum while the summation of these MAC indices is minimum. This criteria is equivalent to having the following sensor distribution index (SDI) to be a minimum

$$\text{SDI} = \max_{i \neq j} \text{MAC}_{ij} \times \frac{\sum_{i \neq j=1}^{m} \text{MAC}_{ij}}{(m^2 - m)} \tag{42}$$

where m is the number of active modes, which happens to be 10 for this synthetic example. Note that this criterion does not guarantee the determination of all 10 modes, as the mode shapes are necessarily partial as a result of the limited number of sensors. By selecting all possible combinations for the five sensors, SDI is calculated using the analytical mode shapes. Figure 13 displays the variation of this index versus sensor combination. As this figure indicates, there are three scenarios that yield the same minimum value for SDI. That is, deploying sensors at 1st, 2nd, 3rd, 5th, 8th or 1st, 4th, 8th, 9th, 10th, or 2nd, 4th, 5th, 6th, 10th would be the best distributions. Here, we use signals recorded at 2nd, 4th, 5th, 6th, and 10th stories, which is one of the equally best three.

The STFD matrices of the response signals are analyzed in the same manner and with the same ϵ_{Grad} and ϵ_{Energy} thresholds as the previous section, in order to automatically select the SATFPs. Figure 14 displays the selected points that are nearly the same as those observed in Figure 5. Again, the best numbers of clusters can be detected by applying the k-means clustering procedure. Figure 15 shows the variation of $\overline{S}$ for a range of k values. The largest value of $\overline{S}$ is obtained with 16 clusters, whose silhouette diagram is shown in Figure 16. To remove the repeated clusters, MAC indices between the centroids of clusters—that is, the identified mode shapes—are used (Figure 17).

Table VI presents the selected clusters, the average ($\overline{s}_i$), the standard deviation of their silhouette values, and their corresponding mode numbers. The MAC indices between these final/identified mode
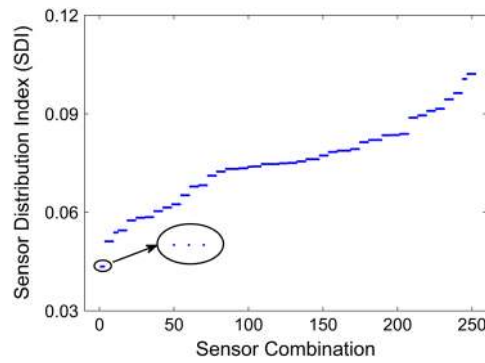
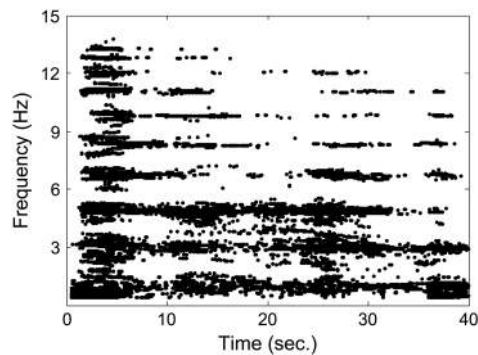Figure 13. Sensor distribution index for all possible combinations.

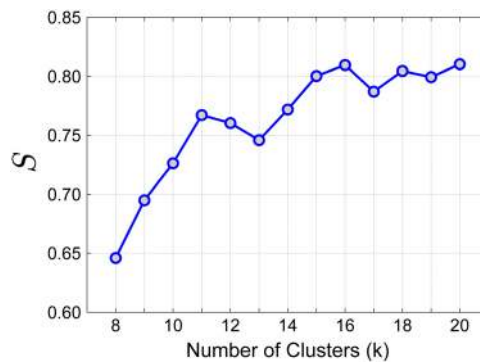

Figure 14. Selected auto-source points.

Figure 15. Variation of $\bar{S}$ with number of clusters.

shapes and their exact counterparts are also shown in this table. As the results indicate, all MAC values are greater than 0.9, which is a better outcome than even the complete instrumentation—lest we forget that these MAC values are calculated using partial mode shapes. To further improve the accuracy of the estimated mode shapes, data with low (here, below-average) silhouette values are removed. The new results are also shown in Table VI as the Second iteration results, wherein the MAC values for a few modes have improved.

Remark 4
The number of sensors cannot be reduced further, because many different modes will look alike at the sensor locations at which point the detection of redundant modes cannot be carried out easily.
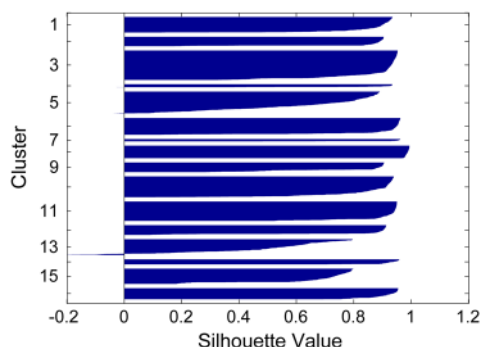
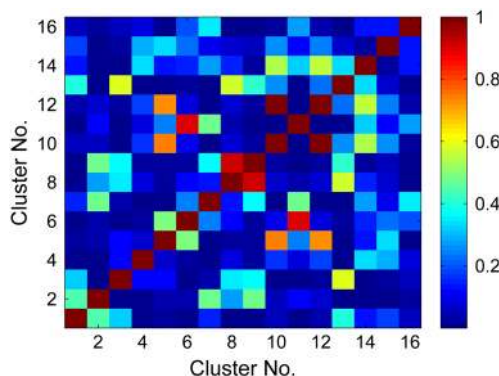Figure 16. Silhouette diagram with 16 clusters.

Figure 17. MAC among the extracted mode shapes.

Figure 18 displays the identified mode shapes from the first and second iterations by red and green solid lines, respectively. In this figure, the clustered and exact mode shapes are also shown by gray and black solid lines, respectively. Note that only the mode shapes at the instrumented floors are shown in Figure 18. As already suggested by the computed MAC values, the identified mode shapes at these floors are nearly exact.

For incomplete instrumentation, it is more appropriate to verify the accuracy of the identified modes through the Coordinate Modal Assurance Criterion (COMAC) [52] index, which is defined for the l-th DOF as

$$\text{COMAC}_l = \frac{\left(\left|\sum_{k=1}^{10} \phi_{kl}^a \phi_{kl}^i\right|\right)^2}{\left(\sum_{k=1}^{10} \phi_{kl}^{a\,2}\right)\left(\sum_{k=1}^{10} \phi_{kl}^{i\,2}\right)} \tag{43}$$

where ϕ_{kl}^a and ϕ_{kl}^i denote the analytical and identified mode shapes, respectively, at the l-th DOF in the k-th mode. Figure 19 displays the COMAC indices for five sensors used in the identification process. As seen there, the mode shapes at the instrumented floors are identified with acceptable accuracy after the first iteration. Nevertheless, the accuracy is improved through the second iteration, especially for the lower stories—except for story 4—whose responses are more affected by the higher modes.

Similar to the complete instrumentation case, we first apply the subspace method on the selected points that are expected to be SATFP. As Figure 20 shows, many points are detected that do not belong to the SATFP category. However, as the mode shapes were identified with suitable accuracy, we continue here with them to recover modal coordinates' TFDs. Figure 21 displays the recovered and the exact modal coordinates' auto-TFDs for modes 2 and 8. Similar to the previous section, the modal coordinates are extracted with satisfactory accuracy, although some error is observed for mode 8. The natural frequencies and the damping ratios are identified through the previously described energy

Table VI. Summary of mode shape identification results.

| Mode no.	1	2	3	4	5	6	7	8	9	10
Cluster no.	3	10	11	9	1	15	2	16	14	4
First iteration										
$\bar{s}_i$	0.878	0.846	0.907	0.788	0.860	0.669	0.840	0.909	0.922	0.861
STDEV	0.132	0.142	0.090	0.188	0.121	0.177	0.165	0.059	0.052	0.168
MAC	0.996	0.927	0.998	0.983	0.994	0.991	0.997	0.997	0.999	0.930
Second iteration										
$\bar{s}_i$	0.935	0.915	0.942	0.892	0.911	0.752	0.888	0.944	0.949	0.924
STDEV	0.016	0.025	0.010	0.018	0.019	0.037	0.017	0.013	0.011	0.017
MAC	0.979	0.963	0.998	0.992	0.984	0.999	1.000	0.994	1.000	0.940
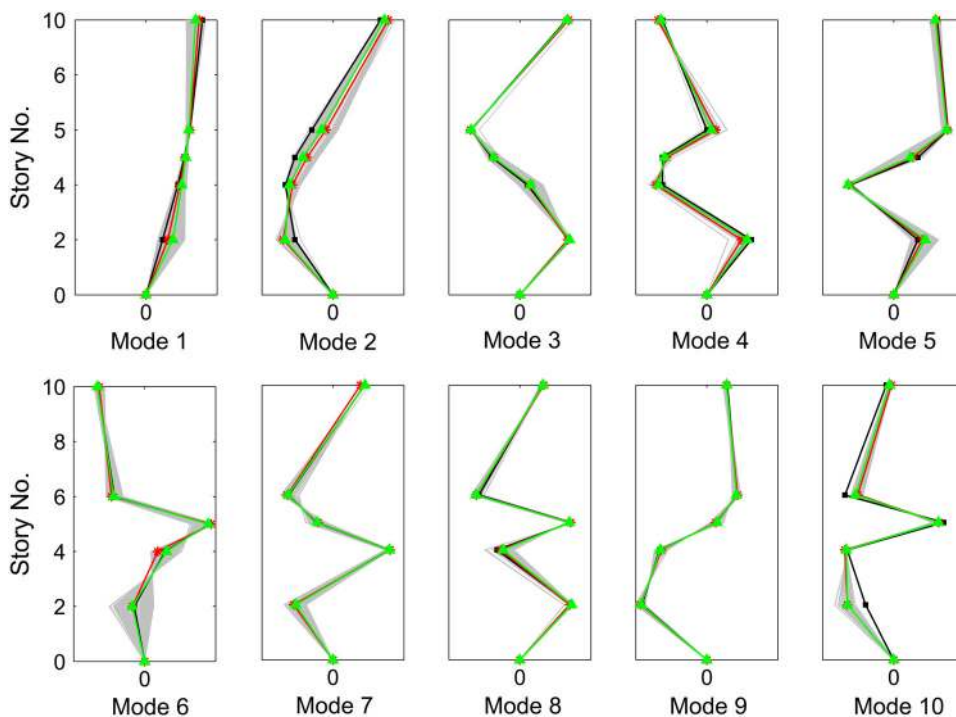
Figure 18. Clustered (gray), exact (black), first estimation (red), and second estimation (green) of mode shapes.
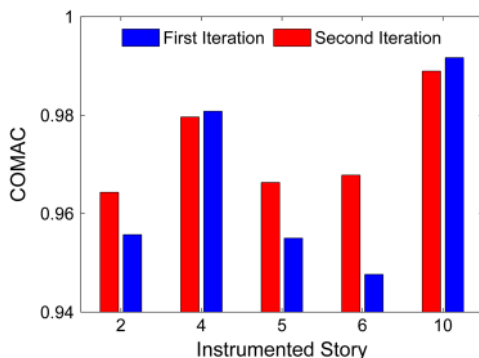

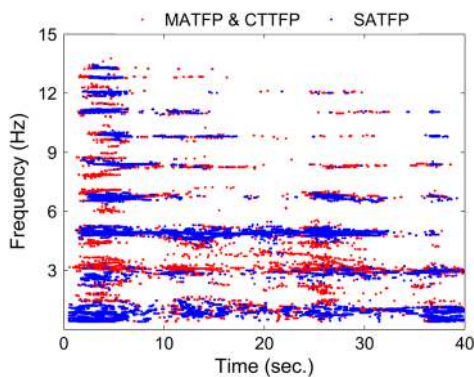Figure 19. COMAC indices for instrumented DOFs in both iterations.

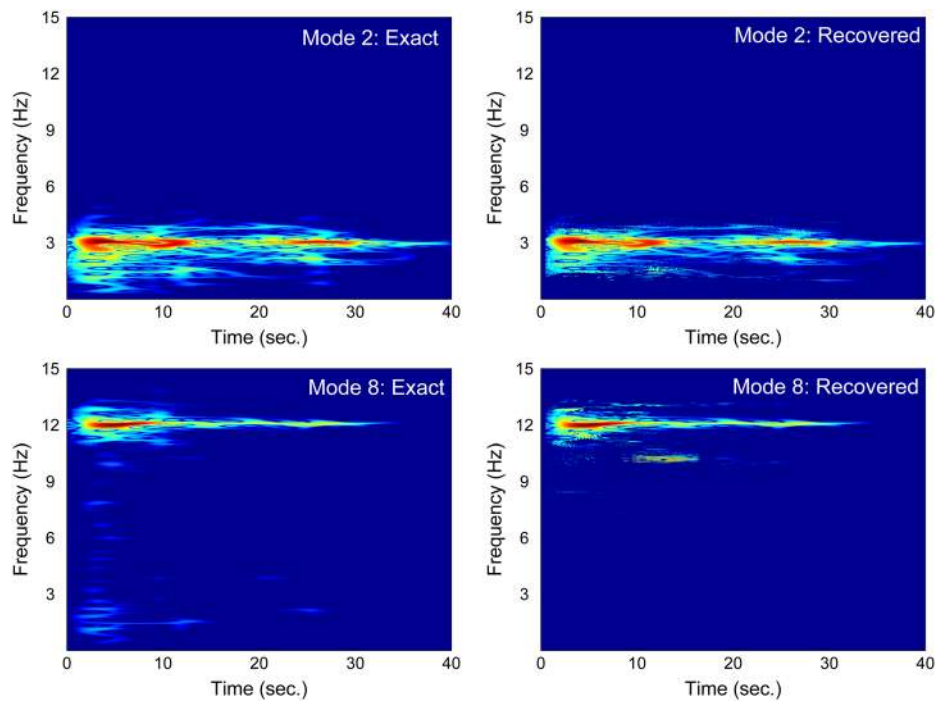Figure 20. Classified selected points as SATFPs and MATFPs or CTTFPs.

Figure 21. Comparison between the auto-TFDs of the exact and the recovered modal coordinates.

Table VII. Identified and exact natural frequencies and damping ratios with incomplete instrumentation.

Mode No.	1	2	3	4	5	6	7	8	9	10
f_i(Hz)	1.04	3.06	4.91	6.74	8.36	9.83	11.05	12.05	12.81	13.24
f_e(Hz)	1.00	2.98	4.89	6.69	8.34	9.81	11.06	12.07	12.79	13.23
$err(\%) = |f_e - f_i|/f_e$	4.00	2.68	0.41	0.75	0.24	0.20	0.09	0.17	0.16	0.08
$\xi_i(\%)$	6.12	1.62	0.98	0.72	0.59	0.49	0.45	0.40	0.38	0.38
$\xi_e(\%)$	5.00	1.68	1.02	0.75	0.60	0.51	0.45	0.41	0.39	0.38
$err(\%) = |\xi_e - \xi_i|/\xi_e$	22.40	3.57	3.92	4.00	1.67	3.92	0.00	2.44	2.56	0.00

index and the curve-fitting process, respectively. For brevity, no graph is presented here for this step, and only the identified results are provided in Table VII, wherein it can be observed that the identified values are almost identical to those extracted by using 10 sensors.

4. CONCLUSIONS

In the present study, a new output-only identification technique was presented with which modal properties—that is, natural frequencies, damping ratios, and mode shapes—can be extracted without having input motions, even when the instrumentation is sparse. This method is an extension of one that is based on a BSS technique that was recently developed by the authors. In the present study, the principal eigenvectors of the STFD matrix of absolute acceleration response signals at automatically selected TF points—named SATFP—are clustered using a *k*-means clustering procedure. The centroids of the each cluster are considered as the mode shapes. Then, the modal coordinates' auto-TFDs are recovered through a subspace approach with which it is possible to detect which modes are present at the TF points. Finally, the natural frequencies and damping ratios are identified from these recovered TFDs. The previously proposed blind identification [11] method was only applicable to systems for which the number of sensors is greater than the number of active modes. The proposed method removes this constraint. Moreover, closely spaced modes are addressed here so that it is not necessary for the modes

to be completely disjointed in the TF domain. Performance of this new technique for both full and sparse instrumentation cases were evaluated through a synthetic data set. The results indicated that the method could be successfully applied to response signals recorded during earthquakes to determine modal parameters using only output motions.

REFERENCES

1. Hart GC, Yao JTP. System identification in structural dynamics. *Journal of Engineering Mechanics (ASCE)* 1976; **103**:1089–1104.
2. Beck JL, Jennings PC. Structural identification using linear models and earthquake records. *Earthquake Engineering and Structural Dynamics* 1980; **8**:145–160.
3. Doebling SW, Farrar CR. The State of the Art in Structural Identification of Constructed Facilities. : Report by the ASCE Committee on Structural Identification of Constructed Facilities, 1999; 115002.
4. Wolf JP. Dynamic Soil-Structure Interaction. Prentice-Hall: Englewood Cliffs, NJ, 1985.
5. Veletsos A, Prasad A. Seismic interaction of structures and soils: stochastic approach. *Journal of Structural Engineering (ASCE)* 1989; **115**(4):935–956.
6. Verhaegen M. Identification of the deterministic part of MIMO state space models given in innovation form from input-output data. *Automatica* 1994; **30**(1):61–74.
7. Van Overschee P, De Moor B. Subspace Identification for Linear Systems: Theory, Implementation, Applications. Kluwer Academic Publishers: Dordrecht, 1996.
8. Juang JN, Pappa RS. An eigensystem realization algorithm for modal parameter identification and model reduction. *Journal of Guidance, Control, and Dynamics* 1985; **8**(5):620–627.
9. James G, Crane T, Lauffer J. The natural excitation technique (NeXT) for modal parameter extraction from operating structures. *Modal Analysis* 1995; **10**:260–277.
10. Brincker R, Zhang L, Andersen P. Modal identification of output-only systems using frequency domain decomposition. *Smart Materials & Structures* 2001; **10**:441–445.
11. Ghahari SF, Abazarsa F, Ghannad MA, Taciroglu E. Response only modal identification of structures using strong motion data. *Earthquake Engineering and Structural Dynamics* 2012. doi:10.1002/eqe.2268.
12. Belouchrani A, Amin MG. Blind source separation based on time-frequency signal representations. *IEEE Transaction on Signal Processing* 1998; **46**(11):2888–2897.
13. Belouchrani A, Abed-Meriam K, Amin MG, Zoubir AM. Blind separation of nonstationary sources. *IEEE Signal Processing Letters* 2004; **11**(7):605–608.
14. Hazra B, Sadhu A, Lourenco R, Narasimhan S. Re-tuning tuned mass dampers using ambient vibration measurements. *Smart Materials and Structures* 2010; **19**(11):115002.
15. Hazra B, Roffel AJ, Narasimhan S, Pandey MD. Modified cross-correlation method for the blind identification of structures. *Journal of Engineering Mechanics* 2010; **136**(7):889–897.
16. Hazra B, Sadhu A, Roffel AJ, Narasimhan S. Hybrid time-frequency blind source separation towards ambient system identification of structures. *Computer-Aided Civil and Infrastructure Engineering* 2012; **27**(5):314–332.
17. Yang Y, Nagarajaiah S. Time-frequency blind source separation using independent component analysis for output-only modal identification of highly-damped structures. *Journal of Structural Engineering* 2012. doi:10.1061/(ASCE)ST.1943-541X.0000621.
18. Sadhu A, Hazra B, Narasimhan S. Blind identification of earthquake-excited structures. *Smart Materials and Structures* 2012; **21**(4):045019.
19. Abazarsa F, Nateghi F, Ghahari SF, Taciroglu E. Blind modal identification of non-classically damped systems from free or ambient vibration records. *Earthquake Spectra* 2013; **29**(3), in press.
20. Hazra B, Sadhu A. Output-only de-tuning assessment of tuned mass dampers. *Journal of Civil Structural Health Monitoring* 2013; **3**(1):33–48.
21. Sadhu A, Narasimhan S. A decentralized blind source separation algorithm for ambient modal identification in the presence of narrowband disturbances. *Structural Control and Health Monitoring* 2013. doi:10.1002/stc.1558.
22. Yang Y, Nagarajaiah S. Blind modal identification of output-only structures in time-domain based on complexity pursuit. *Earthquake Engineering and Structural Dynamics* 2013. doi:10.1002/eqe.2302.
23. Yang Y, Nagarajaiah S. Output-only modal identification with limited sensors using sparse component analysis. *Journal of Sound and Vibration* 2013; **332**(19):4741–3765.
24. Antoni J, Chauhan S. A study and extension of second-order blind source separation to operational modal analysis. *Journal of Sound and Vibration* 2013; **332**(4):1079–1106.
25. Linh-Trung N, Belouchrani A, Abed-Meriam K, Boashash B. Separating more sources than sensors using time-frequency distributions. *EURASIP Journal on Applied Signal Processing* 2005; **17**:2828–2847.
26. Ghahari SF, Ghannad MA, Taciroglu E. Blind identification of soil-structure systems. *Soil Dynamics and Earthquake Engineering* 2013; **45**:56–69.
27. McNeill S. A modal identification algorithm combining blind source separation and state space realization. *Journal of Signal and Information Processing* 2013; **4**:173–185.
28. Aissa-El-Bey A, Linh-Trung N, Abed-Meriam K, Belouchrani A, Grenier Y. Underdetermined blind separation of non-disjoint sources in the time-frequency domain. *IEEE Transaction on Signal Processing* 2007; **55**(3):897–907.
29. Chopra A. Dynamics of Structures: Theory and Applications to Earthquake Engineering. Prentice-Hall: Englewood Cliffs, New Jersey, 1995.
30. Jutten C, Herault J. Space or time adaptive signal processing by neural network models. *Proceedings of AIP Conference*, Lake Louise, Canada, 1986; 206–211.
31. Comon P, Grellier O. Nonlinear inversion of underdetermined mixtures. *ICA'99*, Aussois, France, 1999; 461–465.
32. Bofill P, Zibulevsky M. Underdetermined blind source separation using sparse representations. *Signal Processing* 2001; **81**(11):2353–2362.

33. Yilmaz O, Rickard S. Blind separation of speech mixtures via time-frequency masking. *IEEE Transactions on Signal Processing* 2004; **52**(7):1830–1847.
34. Aissa-El-Bey A, Abed-Meriam K, Grenier Y. Underdetermined blind audio source separation using modal decomposition. *EURASIP Journal on Audio, Speech, and Music Processing* 2007: 15, Article ID 85438.
35. Cohen L. Time-frequency Analysis. Prentice-Hall: Englewood Cliffs, New Jersey, 1995.
36. Boashash B. Time–frequency Signal Analysis and Processing: A Comprehensive Reference. Elsevier Ltd: UK, 2003.
37. Auger F, Flandrin P. Improving the readability of time-frequency and time-scale representations by the reassignment method. *IEEE Transactions on Signal Processing* 1995; **43**:1068–1089.
38. Ville J. Theory and applications of the notion of complex signal. *Cables at Transmissions* 1948; **2A**(1):61–74.
39. Pacific Earthquake Engineering Research Center (PEER). Available from: http://peer.berkeley.edu/smcat/ accessed 07/01/2011.
40. Fevotte C, Doncarli C. Two contributions to blind source separation using time-frequency distributions. *IEEE Signal Processing Letters* 2004; **11**(3):386–389.
41. Giulieri L, Ghennioui H, Thirion-Moreau N, Moreau E. Nonorthogonal joint diagonalization of spatial quadratic time-frequency matrices for source separation. *IEEE Signal Processing Letters* 2005; **12**(5):415–418.
42. Gersho A, Gray RM. Vector Quantization and Signal Compression. Kluwer Academic: Boston, Mass, USA, 1991.
43. Rousseeuw PJ. Silhouettes: a graphical aid to the interpretation and validation of cluster analysis. *Computational and Applied Mathematics* 1987; **20**:53–65.
44. Silhouette (clustering). In Wikipedia, *The Free Encyclopedia*. Available from: http://en.wikipedia.org/w/index.php?title=Silhouette_(clustering)&oldid=490674105.
45. Juang JN, Pappa RS. An eigensystem realization algorithm for modal parameter identification and model reduction. *Journal of Guidance, Control, and Dynamics* 1985; **8**(5):620–627.
46. Van Overschee P, Moor BD. Subspace algorithm for the stochastic identification problem. *Automatica* 1993; **29**(3):649–660.
47. Brincker R, Zhang L, Andersen P. Modal identification of output-only systems using frequency domain decomposition. *Smart Materials and Structures* 2001; **10**:441–445.
48. Yang JN, Lei Y, Pan S, Huang N. System identification of linear structures based on Hilbert-Huang spectral analysis. Part 1: normal modes. *Earthquake Engineering and Structural Dynamics* 2003; **32**:1443–1467.
49. Abazarsa F, Ghahari SF, Nateghi F, Taciroglu E. Response-only modal identification of structures using limited sensors. *Structural Control and Health Monitoring* 2012. doi:10.1002/stc.1513.
50. MATLAB. The Language of Technical Computing. Version 7.0, Mathworks, 2004.
51. Sander J, Ester M, Kriegel H-P, Xu X. Density-based clustering in spatial databases: the algorithm GDBSCAN and its application. *Data Mining and Knowledge Discovery* 1998; **2**:169–194.
52. Lieven NAJ, Ewins DJ. Spatial correlation of mode shapes the coordinate modal assurance criterion (COMAC). *Proceedings of the 6th International Modal Analysis Conference* 1988; **1**:690–695.